

# SOLIDIFICATION CHARACTERISTICS OF EX SITU PARTICULATE-REINFORCED ALUMINUM MATRIX COMPOSITES

**Saeed Farahany** 

Department of Materials, Chemical and Polymer Engineering, Buein Zahra Technical University, Qazvin 3451866391, Iran

**Hamidreza Ghandvar**

Department of Chemical Engineering, New Uzbekistan University, Mustaqillik ave. 54, 100007 Tashkent, Republic of Uzbekistan

**Nur Azmah Nordin**

Malaysia-Japan International Institute of Technology (MJIIT), Universiti Teknologi Malaysia, 54100 Kuala Lumpur, Malaysia

Copyright © 2023 American Foundry Society  
<https://doi.org/10.1007/s40962-023-01005-w>

## Abstract

*This work aimed to elucidate and compare the solidification characteristics of A356.2, A356.2/5% SiC, A356.2/5% Al<sub>2</sub>O<sub>3</sub>, and A356.2/5% ZrO<sub>2</sub> metal composites with and without adding Bi element by using the Fourier thermal analysis method. Microstructural and XRD analysis showed that reinforcement particles have been successfully embedded in the A356.2 alloy through the compo-casting route. Thermal analysis results show that the cooling rate of the A356.2 matrix alloy, as measured in the experimental set-up, was 0.8 °C/s and increased to 1.9 °C/s in the composites. The nucleation temperature of α-Al increased slightly (0.6 °C), and undercooling (8.9–11 °C) was observed for all composites. The nucleation temperature of the Mg<sub>2</sub>Si phase and solidus temperature of composites were lower than the A356.2. Moreover, the growth temperature and recalescence magnitude of eutectic Al-Si*

*did not change remarkably. The solidification temperature range and solidification rate increased by 5% and 33%; however, the solidification time decreased by 21%. The solid fraction at the coherency point increased, which is associated with an expansion in the time difference between nucleation and the coherency point. However, adding Bi resulted in the depression of eutectic growth temperature and the refinement of eutectic Si. These data infer that the solidification kinetic of A356.2 and their composites are identical. It cannot be concluded that reinforcement particle acts as nucleation agents for both α-Al and eutectic Si.*

**Keywords:** aluminum, composite, solidification, thermal analysis, Al<sub>2</sub>O<sub>3</sub>, SiC

## Introduction

Over the past decades, particulate-reinforced aluminum matrix composites (PRAMCs) have attracted the attention of researchers due to their suitable density, high strength, hardness, and high wear resistance at ambient and high temperatures. Therefore, their industrial applications in aerospace, automotive, railway, electronics, and thermal

management have progressed significantly compared to conventional alloys.<sup>1,2</sup> So far, extensive research has been conducted on the fabrication approach to investigate the effect of various incorporated ceramic particles on the microstructure and mechanical properties of PRAMCs. Different routes such as powder metallurgy, [3] milling,<sup>4</sup> pressure infiltration method,<sup>5</sup> ultrasonic cavitation,<sup>6</sup> electromagnetic field,<sup>7</sup> friction stir welding,<sup>8</sup> stir casting,<sup>9,10</sup> and compo-casting<sup>11</sup> have been used to synthesize PRAMCs. The stir casting process is one of the essential routes, mainly due to the lowest costs and easiest ways of

fabrication,<sup>12</sup> in which a distributed phase is mixed with a molten metal through mechanical stirring above the liquidus temperature. The particle incorporation is related to the viscosity of the melt, which is processing temperature-dependent. The compo-casting method is similar to stir casting, in which the particles are integrated into the semi-solid slurry with higher viscosity. Shabani et al.<sup>13</sup> found that compo-casting significantly improves porosity reduction and strength enhancement.

Understanding the solidification characteristics is vital to assessing the microstructure and the performance of PRAMCs. The kinetics of the phase transformations determines microstructural features during their solidification.<sup>14</sup> Depending on the nature of the reinforcement particle and the matrix alloy, there can be effects on the solidification kinetics, i.e., nucleation and growth of the metal matrix.<sup>14</sup>

Thermal analysis studies heat released or required due to phase transformation during solidification. The generated information can be used to discern the latent heat of solidification, the evolution of the fraction solid, the amounts and types of phases that solidify, and even dendrite coherency.<sup>15</sup> Many standardized techniques consist of differential thermal analysis (DTA), differential scanning calorimetry (DSC), thermogravimetry analysis (TGA), and cooling curve analysis (CCA) investigate the solidification behavior of metals and alloys. Although very accurate, DTA, DSC, and TGA techniques require laboratory equipment and are limited to small size and reference samples. The cooling curve analysis (CCA) or cooling curve thermal analysis (CCTA) technique is widely used in monitoring the solidification behavior of monolithic metals and alloys, especially aluminum- and magnesium-based alloys. The obtained curve is called the cooling curve and, together with its derivatives, is employed to characterize the solidification phenomenon. The variation in the nature of the cooling curve always has a significant impact on the microstructure and, consequently, the performance of the material.<sup>16</sup>

It is imaginable that the presence of an insoluble ceramic reinforcement in a liquid metal will induce changes in the liquid-to-solid transformation.<sup>17,18</sup> It is well-known that during solidification, the particles are pushed by the solidification front, engulfed by the solidification front, or act as solid-phase nucleation sites.<sup>19</sup> Moreover, the reinforcement can be a barrier to heat diffusivity, restrict fluid convection, and induce morphological instabilities in the growth front.<sup>20</sup> Formation of the  $Al_5FeSi$  phase<sup>21</sup> and changing the morphology of eutectic  $Si$ <sup>22</sup> affects the thermal conductivity of aluminum-silicon alloys, which are generally used as base alloys for synthesizing composites.

Any change in manufacturing conditions of aluminum metal matrix composites (AMMCs) affects the solidification transformation. Furthermore, solute segregation around the

$SiC$  particles can affect the nucleation and dendritic growth behavior during solidification.<sup>23</sup> Braszczyński et al.<sup>18</sup> determined the solidification kinetics of each phase and nucleation rate in the Al-SiC composite. In addition, variations in the solidification kinetics of A356-SiC composites were examined by using the thermal analysis method.<sup>14</sup> Gonzalez-Rivera et al.<sup>24</sup> found that increasing SiC content significantly increases eutectic growth temperature ( $T_{EG}$ ) and decreases solidification time. Kumar et al.<sup>25</sup> reported a slight increase (2–3 °C) in liquidus temperature and  $T_{EG}$  for A356-TiB<sub>2</sub> composites. Cabrera et al.<sup>17</sup> showed that the volume fraction of SiC particles increases the solid fraction at the dendrite coherency point, DCP, in Al-SiC metal matrix composites. Coherency is the instant during solidification when individual dendrites first impinge upon their neighbors. The crucial factor in semi-solid metal processing is the solid fraction at the forming temperature because it affects the microstructure and mechanical properties of the thixoformed components.<sup>25</sup> Considering the findings in the literature, it is extraordinary that Jeng and Cheng<sup>26</sup> noted that the principal characteristics of the solidification curves of the 6061 and the A356 matrix alloys and their composites are identical.

As pointed out, the metal matrix composites' solidification analysis and crystallization process are complexes.<sup>18</sup> Only a limited and controversial understanding exists regarding the solidification characteristics of AMMCs. This work profoundly explores the influence of ceramic particles with different types, i.e.,  $Al_2O_3$ ,  $ZrO_2$ , and SiC, on the solidification characteristics of AMMCs based on the cooling curve thermal analysis technique. Obtained results are paramount as they indicate the behavior of the composite melt during the solidification process and the effect of adding different types of reinforcements on the characteristic temperature of each phase. A good understanding of the solidification features of the ex situ composites is needed to develop new AMMCs and improve casting processes.

## Experimental Procedure

Table 1 shows the chemical composition of the A356.2 matrix alloy used in this study, obtained by glow discharge spectrometer (LECO GDS-850A). About 500 g of the A356.2 alloy was put into a ceramic crucible and melted in an electrical resistance furnace. After complete melting, the temperature was decreased and kept at  $605 \pm 5$  °C for stirring in a semi-solid state based on the previous study's findings.<sup>27</sup> Following this, a graphite-coated stainless steel stirrer was inserted into the melt and rotated at 600 rpm<sup>28</sup> using a DC motor (Figure 1). Lower speed leads to clustering of reinforcement particles, and higher rotation speed (more than 700 rpm) results in porosity formation in the microstructure. About 5% of SiC,  $Al_2O_3$ , and  $ZrO_2$  preheated at 300 °C was added individually to fabricate A356.2/SiC, A356.2/ $Al_2O_3$ , and A356.2/ $ZrO_2$  composites. Throughout stirring, the temperature was carefully

**Table 1. Chemical Composition of A356.2 Matrix Alloy**

| Element | Si   | Fe   | Cu    | Mn   | Mg   | Ni    | Pb    | Al   |
|---------|------|------|-------|------|------|-------|-------|------|
| wt%     | 7.31 | 0.25 | 0.035 | 0.01 | 0.41 | 0.003 | 0.002 | Bal. |

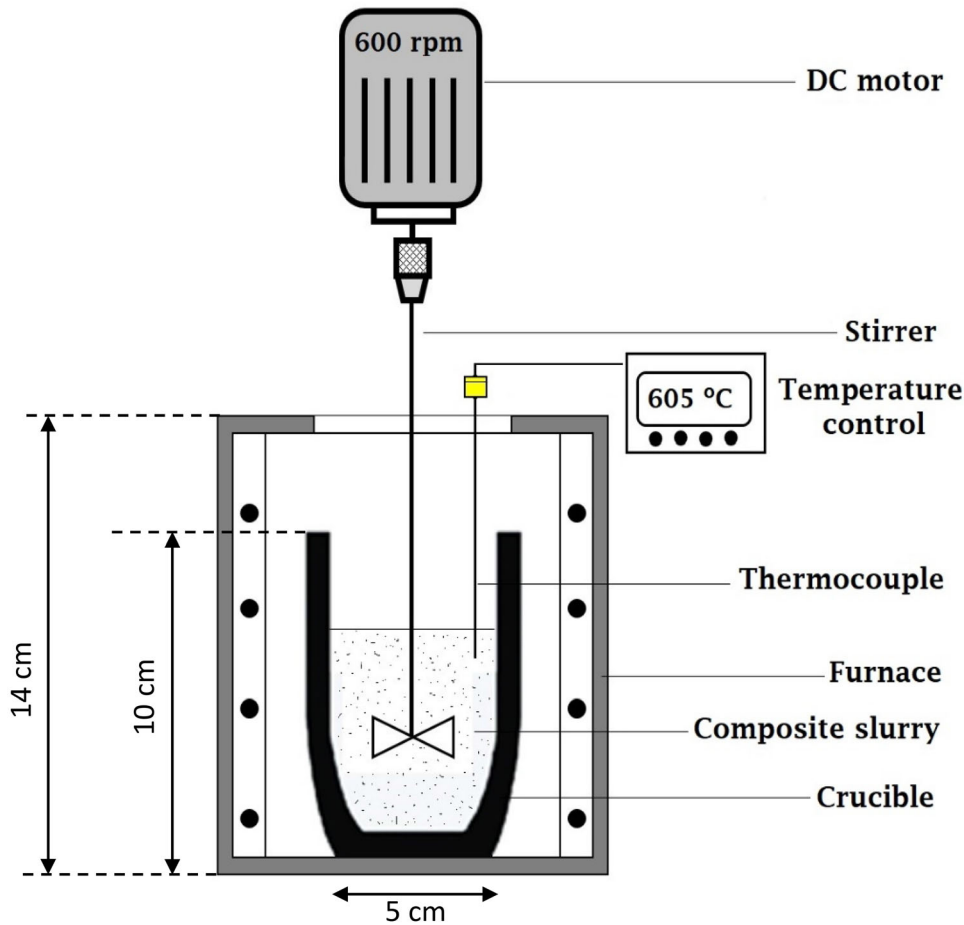


**Figure 1. Schematic set-up for fabrication of composite through compositing route.**

monitored online by a thermocouple positioned in the melt to be sure that process was performed at the exact temperature range ( $605 \pm 5$  °C) and solid fraction percentage required for the compositing operation. A similar procedure was carried out when 0.5 wt% Bi, in pure metallic granules (99.9%), were introduced into the A356.2 matrix alloy before adding reinforcement particles. Bi was added to decrease the surface tension of the liquid matrix alloy. The molten composite was manually stirred for 30 s and immediately cast and poured at  $730 \pm 5$  °C in the cylindrical mold (30-mm diameter and 40-mm height), preheated at 500 °C for 15 min for thermal analysis. Two K-type thermocouples were placed near the center and near the wall, 20 mm above the bottom of the mold. To accurately control the radial heat extraction for the Fourier method, the bottom and top of the mold were insulated. The thermocouples were calibrated before all temperature

measurements. The temperature variations versus time were recorded using high-speed data acquisition modules (KRYPTON DAQ) linked to a laptop with DEWESoft X3 at a 100 Hz/ch dynamic rate. After smoothing with the moving average model, recorded cooling curves and their first and second derivative curves were plotted and analyzed with FlexPro10 data analysis software. At least three thermal analysis runs were made for each condition. Figure 2 shows the cooling curves recorded for the A356.2 matrix alloy presenting the reproducibility of the applied thermal analysis experiment.

For a more precise analysis of the cooling curve and drawing the solid fraction curve, it is essential to plot a curve called zero curve or baseline. It is assumed that the metal does not experience any phase transformation on the zero curve during the solidification process.<sup>29</sup> The zero

curve overlaps the first derivative cooling curve in the single-phase region, before liquidus and after solidus. The zero curve ( $Z_F$ ) was plotted based on the Fourier method, in which it is assumed that heat transfer occurs by conduction. The Fourier technique is more reliable than the Newtonian thermal analysis (NTA) technique.<sup>15,30</sup> The Fourier equation with a heat source can be written as follows:

$$\frac{\partial T}{\partial t} = \alpha \nabla^2 T + \frac{1}{C_V} \frac{\partial Q}{\partial t} \quad \text{Eqn. 1}$$

where  $C_V$  is the volumetric specific heat and  $\alpha$  is the thermal diffusivity. Equation 1 can be written as follows:

$$\frac{\partial Q}{\partial t} = C_V \left( \frac{\partial T}{\partial t} - \alpha \nabla^2 T \right) \quad \text{Eqn. 2}$$

where  $Z_F = \alpha \nabla^2 T$  is the Fourier zero curve. Since a cylindrical mold is used in the current research, the  $\nabla^2 T$  can be calculated as follows:

$$\nabla^2 T = \frac{1}{r} \frac{\partial}{\partial r} \left( r \frac{\partial T}{\partial r} \right) \quad \text{Eqn. 3}$$

Considering a cylindrical mold with known temperatures at radii  $R_1$  and  $R_2$  in the test sample,

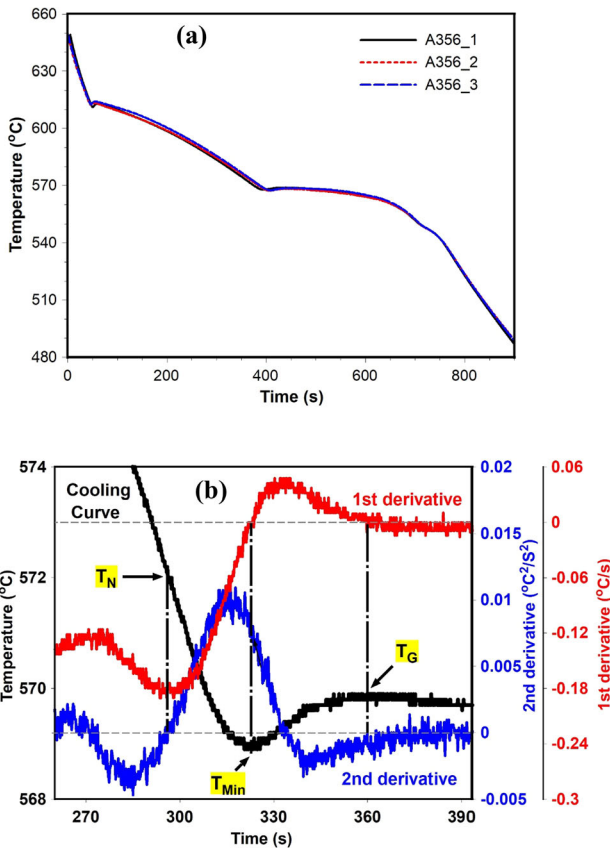


**Figure 2. (a) Cooling curves of A356.2 matrix alloy after three repetitions of the thermal analysis test. (b) The graphical expression of the method used to determine the characteristic temperature.**

$\nabla^2 T$  can be calculated from Eqn. 3 as follows:

$$\nabla^2 T = \frac{4(T_2 - T_1)}{R_2^2 - R_1^2} \quad \text{Eqn. 4}$$

where  $T_1$  and  $T_2$  are temperatures at radii  $R_1$  and  $R_2$ , respectively. Samples for metallography were selected near the tip of the thermocouple. Specimens were ground, polished with silica (OPS—0.3 mm), and finally etched with Keller's reagent. XRD was conducted (Siemens-D500) using Cu  $K\alpha$  line generated at 40 kV and 35 mA to identify reinforcement particles in the matrix alloy. The microstructures were analyzed using an optical microscope (Nikon-MIDROPHOT-FXL).

## Results and Discussion

### Cooling Curves

Figure 3a shows the assembly of all recorded cooling curves of the A356.2 matrix alloy and synthesized composites collected from the thermocouples at the center.

It should be noted that for better readability, the curves have been shifted in the time axis. However, the individual cooling curves started at zero. The cooling curves reflect the difference in the solidification behavior of the samples after the addition of SiC,  $Al_2O_3$ , and  $ZrO_2$  reinforcements

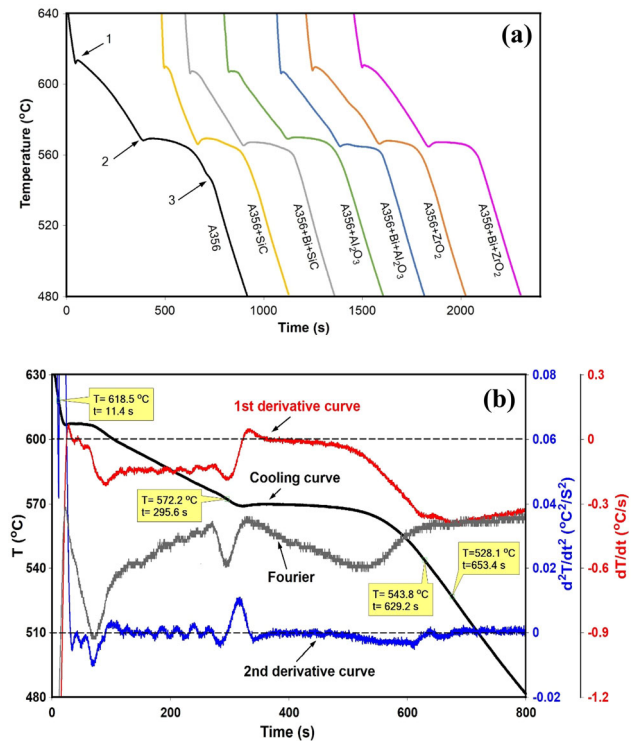


**Figure 3. (a) Cooling curves of the A356.2 matrix alloy and synthesized composites and (b) cooling curve of A356.2/ $Al_2O_3$  composite with corresponding 1st and 2nd derivatives curves and Fourier baseline.**

and Bi addition. In general, regarding the slope changes on the cooling curves, three different phase transformations can be seen, indicated by arrows on the cooling curve of the A356.2 matrix alloy. The first phase reaction is related to forming the aluminum phase ( $\alpha$ -Al phase), and the second is associated with the evolution of the eutectic Al-Si phase. The  $Mg_2Si$  intermetallic can also be seen on the cooling curve as the last phase. Although, it is more challenging to recognize than the previous two phases. The first and second derivative curves are plotted to accurately identify each phase formation characteristic (Figure 3b). For each phase transformation during solidification, when the temperature drops below nucleation temperature,  $dT/dt$  shifts up due to the increase of nucleation rate. After minimum temperature, the evolution of latent heat from primary nuclei causes it to reheat until the melt till starting coarsening step.

## Phase Reactions

The segments related to the phase reactions of  $\alpha$ -Al, eutectic Al-Si, and  $Mg_2Si$  phase transformations are plotted separately in Figure 4. Figure 4a shows the temperature changes during the aluminum precipitation in more detail. The cooling rate is measured from the slope of the cooling curve in this area, between the pouring temperature and first phase formation temperature, i.e., nucleation temperature of  $\alpha$ -Al or liquidus temperature. The cooling rate in the A356.2 matrix alloy was found to be 0.8 °C/s. However, the cooling rate of composite samples increased to 1.9 °C/s.

It is clear from Figure 4a that the  $\alpha$ -Al transformation characteristics have been changed after adding SiC,  $Al_2O_3$ , and  $ZrO_2$  reinforcements with and without Bi addition. Nucleation temperature ( $T_N$ ) of the  $\alpha$ -Al and undercooling ( $\Delta T$ ), which is defined as the difference between  $T_N$  and minimum temperature ( $T_{Min}$ ), are two critical parameters

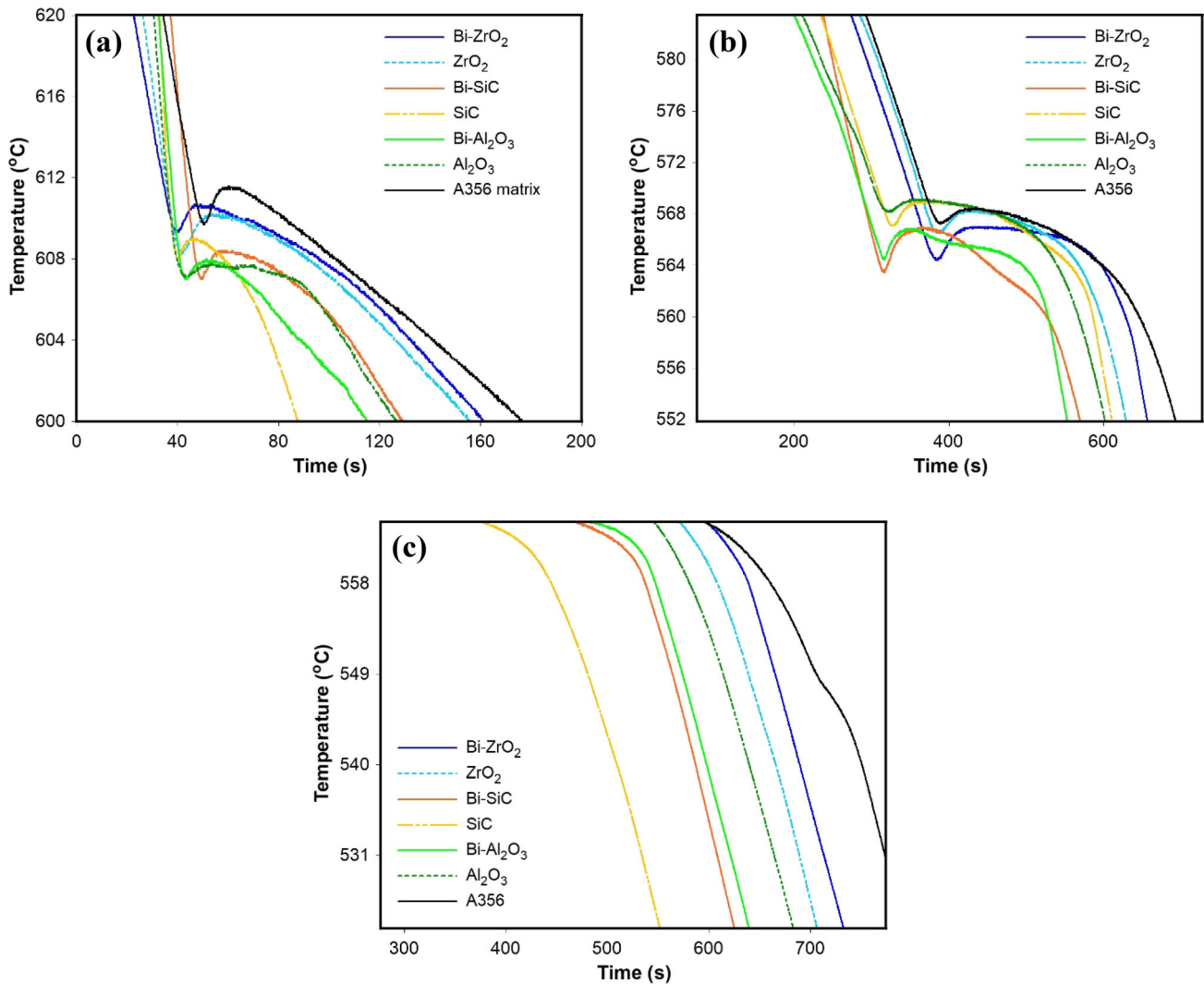


**Figure 4.** Three sections for transformations of (a)  $\alpha$ -Al, (b) Al-Si, and (c)  $Mg_2Si$  phases for matrix alloy and fabricated composites.

**Table 2. Characteristic Parameters for Each Phase Reaction of the Matrix and the Fabricated Composites During Solidification**

| Samples                                  | Parameter | $\alpha$ -Al dendrite |           |       | DCP   | $T_N - T_{DCP}$ | Eutectic Al-Si |            |          | $T_N$ (Mg <sub>2</sub> Si) | Solidus |
|--|-----------|-----------------------|-----------|-------|-------|-----------------|----------------|------------|----------|----------------------------|---------|
|  |           | $T_N$                 | $T_{Min}$ | $T_G$ |       |                 | $T_{EN}$       | $T_{EMin}$ | $T_{EG}$ |                            |         |
| A356.2                                   | T (°C)    | 618.3                 | 608.9     | 611.5 | 607.8 | 10.5            | 570.5          | 567.5      | 568.6    | 550.7                      | 532.7   |
|  | t (s)     | 31.7                  | 44.8      | 54.5  | 80.3  | 48.7            | 364.4          | 387.6      | 432.7    | 697.8                      | 774.3   |
| A356.2/SiC                               | T (°C)    | 618.4                 | 609.5     | 609   | 606   | 12.4            | 571.1          | 567.4      | 568.9    | 543.8                      | 530.2   |
|  | t (s)     | 8.3                   | 14.9      | 21    | 60.9  | 52.6            | 213.8          | 184.7      | 229      | 472.6                      | 570.8   |
| A356.2+Bi/SiC                            | T (°C)    | 618.9                 | 609.2     | 608.4 | 606.9 | 12              | 567.5          | 564.2      | 567.1    | 545.9                      | 531.1   |
|  | t (s)     | 14.9                  | 26.5      | 34.9  | 66.6  | 51.7            | 280.9          | 296.3      | 327.7    | 563.8                      | 616     |
| A356.2/Al <sub>2</sub> O <sub>3</sub>    | T (°C)    | 618.5                 | 608.1     | 607.8 | 606.6 | 11.9            | 572.2          | 568.2      | 569.1    | 543.8                      | 528.1   |
|  | t (s)     | 11.4                  | 22.9      | 33.1  | 65.4  | 49.1            | 295.6          | 321.2      | 349.4    | 629.2                      | 653.4   |
| A356.2+Bi/Al <sub>2</sub> O <sub>3</sub> | T (°C)    | 618.9                 | 607.9     | 608   | 606.4 | 12.5            | 570            | 564.4      | 566.9    | 542.6                      | 528.9   |
|  | t (s)     | 12.9                  | 22.6      | 31.5  | 71.7  | 58.8            | 292            | 304.2      | 341.3    | 571.1                      | 641.6   |
| A356.2/ZrO <sub>2</sub>                  | T (°C)    | 618.5                 | 608.3     | 610.2 | 606.8 | 11.7            | 571.1          | 566.7      | 568.2    | 548.8                      | 530.1   |
|  | t (s)     | 32.9                  | 47.1      | 59.2  | 90.1  | 57.3            | 358.3          | 385.8      | 420.5    | 636.9                      | 691.4   |
| A356.2+Bi/ZrO <sub>2</sub>               | T (°C)    | 618.6                 | 609.2     | 610.6 | 606.4 | 12.2            | 567.8          | 564.7      | 567.2    | 547.5                      | 530.7   |
|  | t (s)     | 32.6                  | 47.3      | 54.9  | 92.3  | 59.7            | 361.7          | 383.3      | 436      | 669.4                      | 711.5   |

used to predict microstructural changes, especially grain refinement of  $\alpha$ -Al. Variations of  $T_N$ ,  $T_{Min}$ , and  $T_G$  for  $\alpha$ -Al precipitation are given in Table 2. The liquidus temperature of composites appears to be lower due to decreased thermal conductivity of the composite melt and increased temperature gradient within the specimen.<sup>16</sup> However, the presented results in the literature are not consistent. It can be seen that  $T_N$  for matrix alloy is 618.3 °C which almost remained constant at 618.4 °C for A356.2/SiC and then slightly increased to 618.9 °C for A356.2+Bi/SiC composites. In addition, this value is 618.5 °C and 618.9 °C for A356.2/Al<sub>2</sub>O<sub>3</sub> and A356.2+Bi/Al<sub>2</sub>O<sub>3</sub> composites, respectively.  $T_N$  was measured at 618.5 °C and 618.6 °C for A356.2/ZrO<sub>2</sub> and A356+Bi/ZrO<sub>2</sub> composites, respectively. As is shown, the maximum change in  $T_N$  is 0.6 °C. Jeng and Cheng<sup>26</sup> found only a 2 °C difference in  $T_N$  even after adding 15% and 20% Al<sub>2</sub>O<sub>3</sub> (3–4 times more than current research). As can be seen, the  $T_N$  is slightly higher for all fabricated composites than that of A356.2 matrix alloy, although it is negligible.  $\Delta T$  indicates the barrier for nucleation of the  $\alpha$ -Al phase. Calculation of undercooling shows that the magnitude of  $\Delta T$  for A356.2 alloy is 9.4 °C, decreasing to the 8.9 °C and then increasing to 9.7 °C for A356.2/SiC and A356.2+Bi/SiC composites, respectively. The  $\Delta T$  was measured at 10.4, 11, 10.2, and 9.2 °C for A356.2/Al<sub>2</sub>O<sub>3</sub>, A356.2+Bi/Al<sub>2</sub>O<sub>3</sub>, A356.2/ZrO<sub>2</sub>, and A356.2+Bi/ZrO<sub>2</sub> composites, respectively. In addition, contrary to the results presented in,<sup>25</sup> the undercooling of most composite samples is even higher than the matrix alloy. It can be related to the absence of nucleation of the  $\alpha$ -Al on the SiC particles reported in the previous work.<sup>14</sup> Moreover, Bi did not significantly affect the  $\Delta T$  parameter of  $\alpha$ -Al phase.

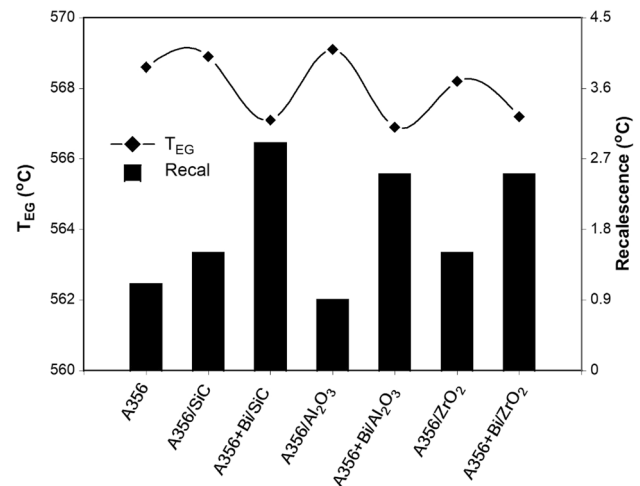


**Figure 5. Variations of growth temperature and recalescence magnitude of eutectic Al-Si reaction in matrix alloy and composites.**

Figure 4b shows the precipitation segment of the Al-Si eutectic phase. Eutectic growth temperature ( $T_{EG}$ ) and recalescence magnitude ( $T_{EG} - T_{Min}$ ) are used to assess eutectic Si morphology. The variation of  $T_{EG}$  is shown in Figure 5. It can be seen that the  $T_{EG}$  is 568.6 °C for the A356.2 alloy, which increased slightly to 568.9 °C and 569.1 °C for A356.2/SiC and A356.2/Al<sub>2</sub>O<sub>3</sub> composites, respectively. However,  $T_{EG}$  remained constant for A356.2/ZrO<sub>2</sub> composite at 568.6 °C. Gowri et al.<sup>31</sup> and Gonzalez et al.<sup>24</sup> observed that the  $T_{EG}$  of composites was higher than that of the Sr-modified A356 matrix alloy at all cooling rates. It has been reported that increased  $T_{EG}$  could be associated with the nucleation of eutectic Si on SiC

particles.<sup>14,26</sup> However, according to Figure 5, the variations of the  $T_{EG}$  are not adequate to change the solidification kinetic of the eutectic Al-Si phase for all composites. Referring to,<sup>26</sup> the principal characteristics of th6061 and A356 composite solidification and their matrix alloy are identical.

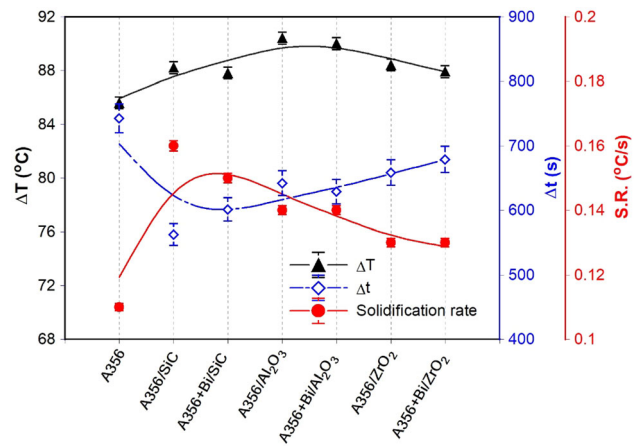
On the other hand, adding Bi decreased the  $T_{EG}$  for all composites regardless of the reinforcing particle type.  $T_{EG}$  decreased from 568.9 to 567.1 °C for A356.2+Bi/SiC composite.  $T_{EG}$  for A356.2/Al<sub>2</sub>O<sub>3</sub> composite was at 569.1 °C, which fell by 2.2 °C after adding Bi. Moreover, after adding Bi to the A356/ZrO<sub>2</sub> composite,  $T_{EG}$  was reduced to 567.2 °C. The lowest  $T_{EG}$  was obtained for A356.2+Bi/Al<sub>2</sub>O<sub>3</sub>. In addition, as can be seen, the recalescence magnitude for composite containing Bi is higher than the A356 matrix and composites without Bi. The recalescence for A356.2+Bi/SiC, A356.2+Bi/Al<sub>2</sub>O<sub>3</sub>, and A356.2+Bi/ZrO<sub>2</sub> is 2.9 °C, 2.5 °C, and 2.5 °C, respectively. It is believed that a depression in  $T_{EG}$  and an increase in recalescence are attributed to the modification level of eutectic Si.<sup>32,33</sup>

Figure 4c shows the formation of the intermetallic Mg<sub>2</sub>Si segment. The variations in the nucleation temperatures for the Mg<sub>2</sub>Si phase are shown in Table 2. The  $T_N$  for Mg<sub>2</sub>Si was 550.7 °C for the A356.2 alloy. The nucleation temperature is lower for fabricated composites than matrix alloy. The lowest temperature was measured at 542.6 °C for A356.2+Bi/Al<sub>2</sub>O<sub>3</sub>. In addition, the variations of solidus temperature, the point where remained liquid was transformed entirely into a solid, are given in Table 2. It can be seen that the solidus temperature of the A356.2 matrix alloy was 532.7 °C, which fluctuated between 528.1 and 531.1 °C after the addition of reinforcement particles.

## Solidification Range

The solidification temperature range ( $\Delta T_R$ ) and solidification duration ( $\Delta t_R$ ) are measured based on the temperature and time in the beginning (liquidus) and the end of solidification (solidus). Both are vital parameters, especially for thixo- and rheo-casting. Figure 6 demonstrates that the solidification range for A356.2 alloy is 85.6 °C. As can be seen, the  $\Delta T_R$  is wider in all fabricated composites than in the matrix. The lowest  $\Delta T_R$  was recorded at 86.9 °C for both A356.2+Bi/SiC and A356.2+Bi/ZrO<sub>2</sub> composites. However, the highest  $\Delta T_R$  was measured at 89.4 °C for A356.2+Bi/Al<sub>2</sub>O<sub>3</sub> composite.

Regarding solidification time,  $\Delta t_R$ , the duration of the matrix alloy was 742.6 s. As shown from Table 2, the solidification of the fabricated composite is completed sooner. The shortest duration time belongs to the A356.2+Bi/Al<sub>2</sub>O<sub>3</sub> composite for 570.8 s. The A356.2/ZrO<sub>2</sub> composite took the most extended (658.6 s) but was still 11% less than the A356.2 matrix alloy.



**Figure 6. Solidification temperature range ( $\Delta T_R$ ), solidification duration ( $\Delta t_R$ ), and solidification rate (SR) for the matrix alloy and synthesized composites.**

Gonzalez-Rivera et al.<sup>34</sup> and Hanumanth et al.<sup>35</sup> also reported a shortening of cooling time for the A356 matrix reinforced with SiC particles. The reinforcement particles do not show phase transformations during composite processing. So, there is a decrease in the latent heat released during the solidification of the composite and, consequently, a reduction in the solidification time.<sup>14</sup> Furthermore, the quantity of liquid metal per unit volume decreases after adding reinforcement particles, reducing the solidification heat amount. Therefore, composite solidification time is shorter than matrix.<sup>18</sup>

To summarize this section, the solidification rate, which is affected by both the temperature range and time, was evaluated as a parameter showing the behavior of the composite in the semi-solid region. The solidification rate is vital since the mushy zone is vigorous in the thixo-forming process. The solidification rate (SR) can be calculated as follows:

$$SR = \Delta T_R / \Delta t_R \quad \text{Eqn. 5}$$

Figure 6 demonstrates that the SR for the A356.2 alloy is 0.12 °C/s which increased to 0.16 °C/s for A356.2/SiC and A356.2+Bi/SiC composites. The SR was 0.14 °C/s for both A356.2/Al<sub>2</sub>O<sub>3</sub> and A356.2+Bi/Al<sub>2</sub>O<sub>3</sub>. This value was calculated at 0.13 °C/s for A356.2/ZrO<sub>2</sub> and A356.2+Bi/ZrO<sub>2</sub> composites. It can be attributed to the decrease in the latent heat released during the solidification of composites in which composite melt solidifies faster. Since the duration variation is much more than the solidification range, the role of time is more significant than the temperature.

On the other hand, it is worth noting that the CR and SR show different trends during the solidification of composites. Although the CR is equal for fabricated composites (1.9 °C/s), the SR is dissimilar. This may be related to the particles' nature, distribution, and thermophysical

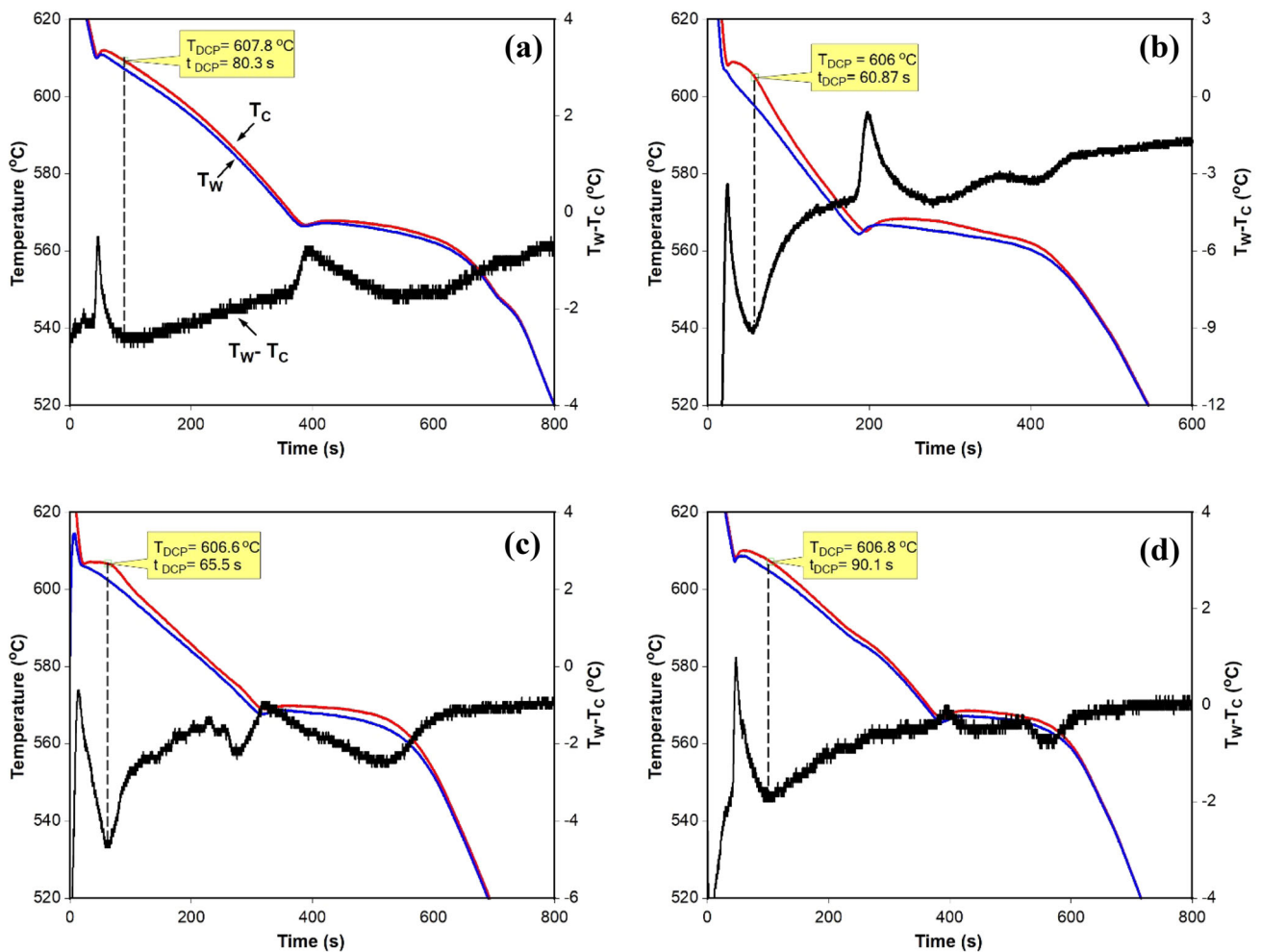


**Figure 7. Cooling curves recorded by the center ( $T_C$ ) and wall ( $T_W$ ) thermocouples and corresponding  $T_W - T_C$  for (a) A356.2 matrix alloy, (b) A356.2/SiC, (c) A356.2/Al<sub>2</sub>O<sub>3</sub>, and (d) A356.2/ZrO<sub>2</sub> composites.**

properties,<sup>35</sup> which affect the solidification phenomenon of metal matrix composites. Moreover, it was found that the SR is almost similar to the familiar composite. No significant changes were observed after the addition of Bi.

### Coherency Characteristics

Coherency is defined as the point at which dendritic networks touch each other, which is along with hindering the melt flow. Determination of DCP is important as casting defects such as macro-segregation, shrinkage porosity, and hot tearing begin to develop. The first minimum difference between the thermocouple at a nearby inner wall ( $T_W$ ) and the center ( $T_C$ ) after nucleation of  $\alpha$ -Al was considered for the dendrite coherency determination due to the higher thermal conductivity of the solid. Figure 7 shows the cooling curves of the A356.2 matrix alloy, A356.2/SiC, A356.2/Al<sub>2</sub>O<sub>3</sub>, and A356.2/ZrO<sub>2</sub> composites recorded by  $T_C$  and  $T_W$  thermocouples and its projection on the  $T_C$  cooling curve to determine the DCP and the corresponding temperature and time,  $T_{DCP}$  and  $t_{DCP}$ , respectively.  $T_{DCP}$ ,  $t_{DCP}$ , and solid

fraction at DCP are associated with grain size. In the case of dendritic solidification, free dendrite does not touch one another, and the dendrite thickens after dendrite coherency. As shown in Figure 7a, the  $T_{DCP}$  of matrix alloy is 607.8 °C. Moreover, the coherency of A356.2/SiC, A356.2/Al<sub>2</sub>O<sub>3</sub>, and A356.2/ZrO<sub>2</sub> occurred at 606 °C, 606.6 °C, and 606.8 °C, respectively (Figure 6b–d). Figure 8 presents the variations of the coherency temperature and time for matrix alloy and synthesized composites.  $T_{DCP}$  is lower for all composites than that of the matrix alloy.

Moreover, adding Bi into the composites slightly increased the  $T_{DCP}$  in A356.2+Bi/SiC and decreased it in A356.2/Al<sub>2</sub>O<sub>3</sub> and A356.2/ZrO<sub>2</sub>. Chai et al.<sup>36</sup> emphasized the  $t_{DCP}$  and proposed that grain size is inversely proportional to coherency time. As shown in Figure 8, A356.2/SiC and A356.2/Al<sub>2</sub>O<sub>3</sub> composites show lower  $t_{DCP}$ , but A356.2/ZrO<sub>2</sub> presents higher  $t_{DCP}$  than the matrix alloy.

Since there is no specific basis for measuring the temperature and time at the coherency point, and these two criteria can differ based on the time and temperature of the



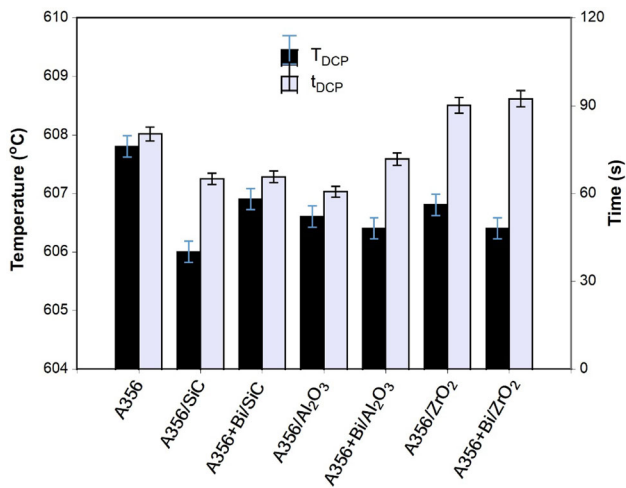


**Figure 8. Variations of temperature and time at DCP for the A356.2 matrix alloy and synthesized composites.**

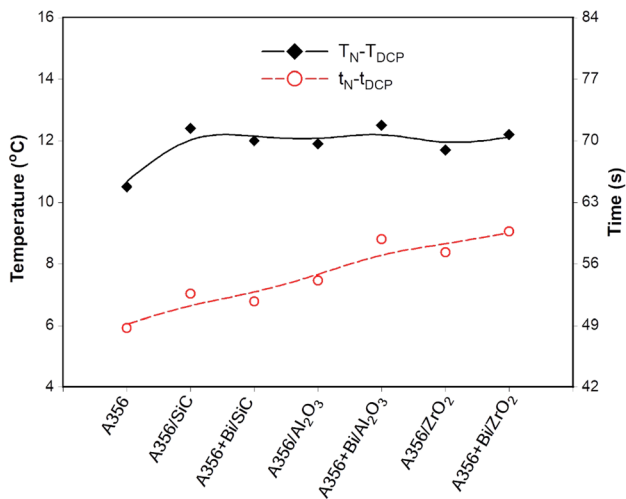


**Figure 9. Variations of  $T_N - T_{DCP}$  and  $t_N - t_{DCP}$  for the A356.2 matrix alloy and synthesized composites.**

recording, the difference between the beginning of solidification and the coherency point ( $T_N - T_{DCP}$  and  $t_N - t_{DCP}$ ) is a more accurate criterion for investigation. This difference corresponds to free dendritic growth, while after DCP, it corresponds to dendrite thickening, resulting in a fixed dendritic skeleton<sup>37</sup>. Figure 9 illustrates the variations of  $T_N - T_{DCP}$ . It can be seen that this difference is 10.5 °C for matrix alloy, which reached the highest at 12.5 °C for A356.2+Bi/Al<sub>2</sub>O<sub>3</sub> composite. The range of changes is limited to around 2 °C.

On the other hand, the  $t_N - t_{DCP}$  is 48.7 s for A356.2 alloy, which increased to 52.6 s and 51.7 s for A356.2/SiC and A356.2+Bi/SiC composite, respectively. The longest  $t_N - t_{DCP}$  was measured at 59.7 s for A356.2+Bi/ZrO<sub>2</sub> composite. As shown in Figure 9, the  $t_N - t_{DCP}$  for all composites is higher than matrix alloy. It means that the contact of dendrites is delayed. Therefore, smaller grain touches each other later.

### Solid Fraction at DCP

The solid coherency fraction solid is one of the most critical parameters in the alloy solidification process, which is related to the flow stoppage of molten metal.<sup>38</sup> The integrated area between the first derivative curve and baseline was calculated to measure the solid fraction curve. The baseline variation represents phase evolution during solidification and displays as the first derivative curve trend. Figure 10a shows the cooling curve (CC) and corresponding solid fraction curve ( $f_s$ ) for the A356.2 matrix alloy. As can be seen, the  $f_s$  of A356.2 at DCP is 16%. The  $f_s$  remained constant at 16% for A356.2/SiC composite.

Moreover, compared to the A356.2 alloy, the  $f_s$  increased slightly to 18% and 17% for A356.2/Al<sub>2</sub>O<sub>3</sub> and A356.2/ZrO<sub>2</sub> composite, respectively. Obtained results agree with Cabrera's et al.<sup>17</sup> findings. The reinforcement particles affect the solidification kinetics of the primary  $\alpha$ -Al phase. However, this effect is relatively small compared to the grain refinement reagent, i.e., AlTiB and TiC. An increase of  $f_s$  at coherency can be associated with the longer  $t_N - t_{DCP}$  while the dendrite touches each other later.

Additionally, this may be caused by reinforcement acting during solidification as a physical barrier to solute diffusion.<sup>20</sup> This could decrease the solute gradient and the dendrite tips' local velocity growing in the particles' immediate neighborhood.<sup>17</sup> On the other hand, adding Bi did not affect the  $f_s$  at DCP for all composites. The  $f_s$  remained almost constant after adding Bi into the fabricated composites.

### Microstructural Characterization

Composite samples were analyzed by X-ray diffraction (XRD) to evaluate the incorporation of reinforcement particles in the A356.2 matrix. Figure 11 shows the X-ray spectra of the A356.2/SiC, A356.2+Bi/SiC, A356.2/Al<sub>2</sub>O<sub>3</sub>, A356.2+Bi/Al<sub>2</sub>O<sub>3</sub>, A356.2/ZrO<sub>2</sub>, and A356.2+Bi/ZrO<sub>2</sub> composites. The name of each phase is mentioned next to the matched peak. In addition to the main phase, Al and Si, the peaks corresponding to the SiC, Al<sub>2</sub>O<sub>3</sub>, and ZrO<sub>2</sub> phases, along with Bi, were detected. In addition, analyses of the results verified the integration of particles in A356.2 alloy before and after adding Bi.

Figure 12 shows the microstructure of the A356.2 matrix alloy, A356.2/SiC, A356.2+Bi/SiC, A356.2/Al<sub>2</sub>O<sub>3</sub>, A356.2+Bi/Al<sub>2</sub>O<sub>3</sub>, A356.2/ZrO<sub>2</sub>, and A356.2+Bi/ZrO<sub>2</sub> composites. Based on the recorded cooling curve presented in Figure 3a, the microstructure of the A356.2 has two main phases:  $\alpha$ -Al and eutectic Al-Si (Figure 12a). Evaluation of solidification parameters, i.e., nucleation temperature, undercooling magnitude, coherency temperature, and solid fraction at DCP, showed that the presence of reinforcement particles has no remarkable impact on the

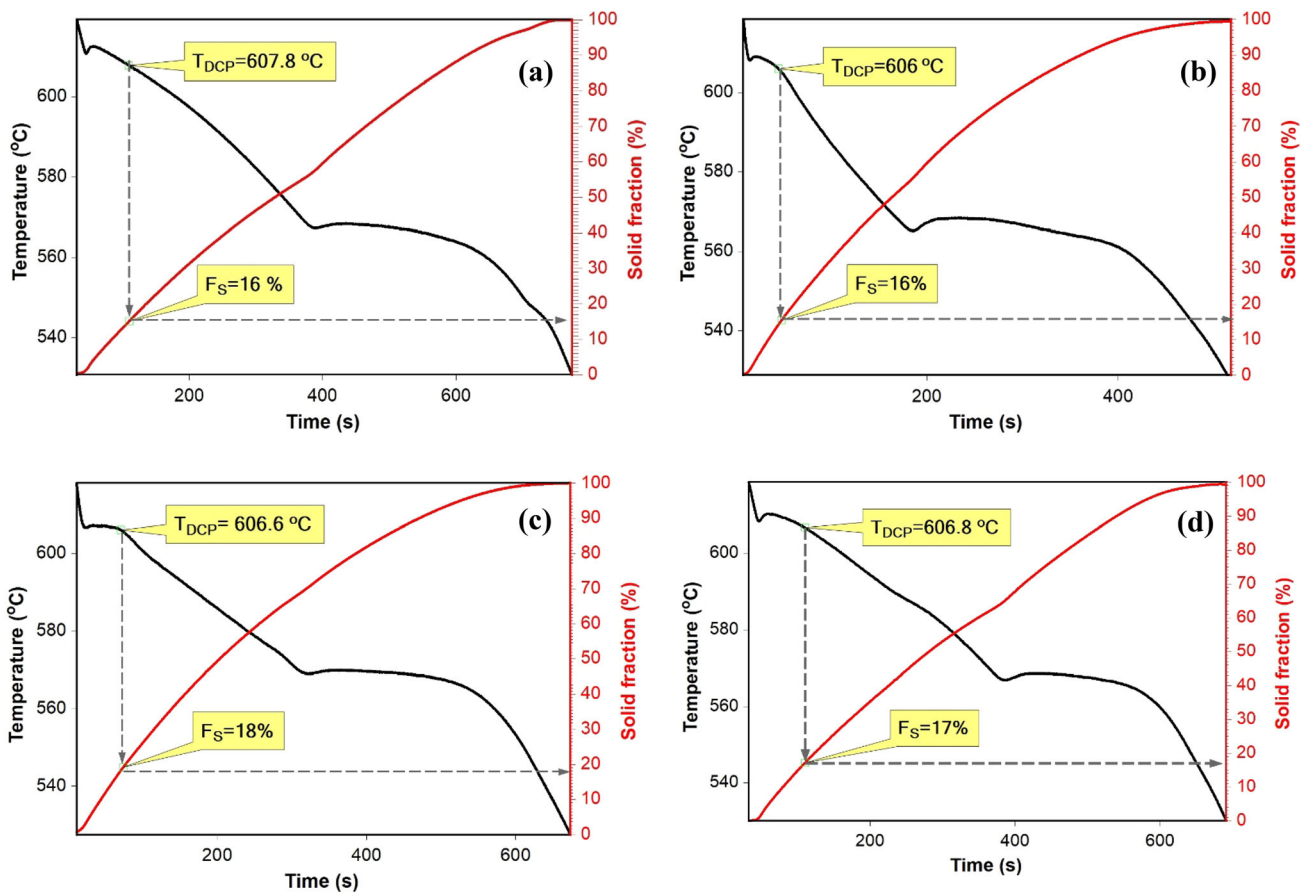


Figure 10. Cooling curves and corresponding solid fraction curve for (a) A356.2 matrix alloy, (b) A356.2/SiC, (c) A356.2/Al<sub>2</sub>O<sub>3</sub>, and (d) A356.2/ZrO<sub>2</sub> composites.

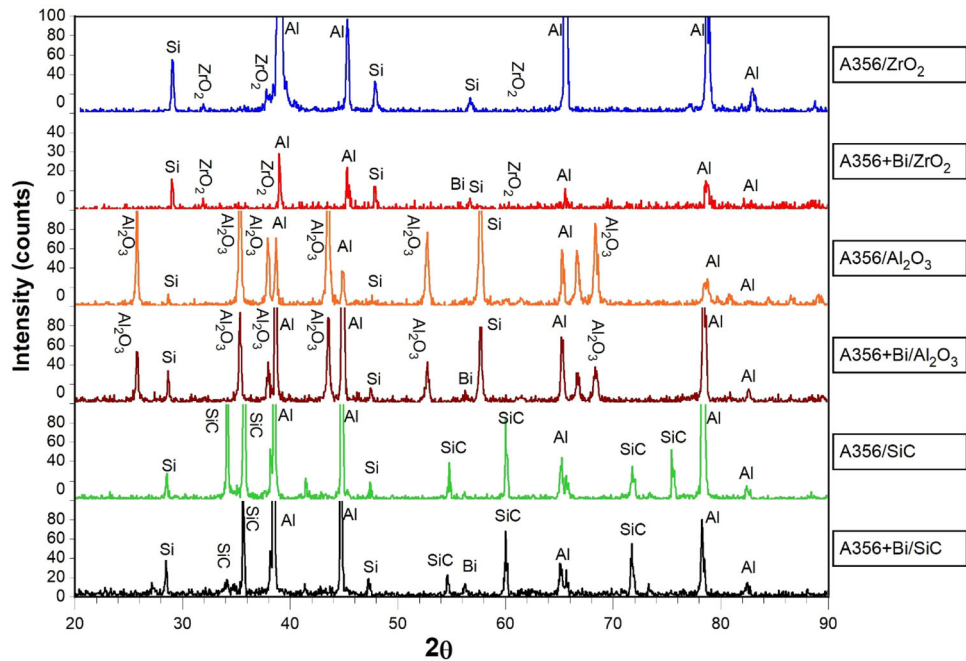
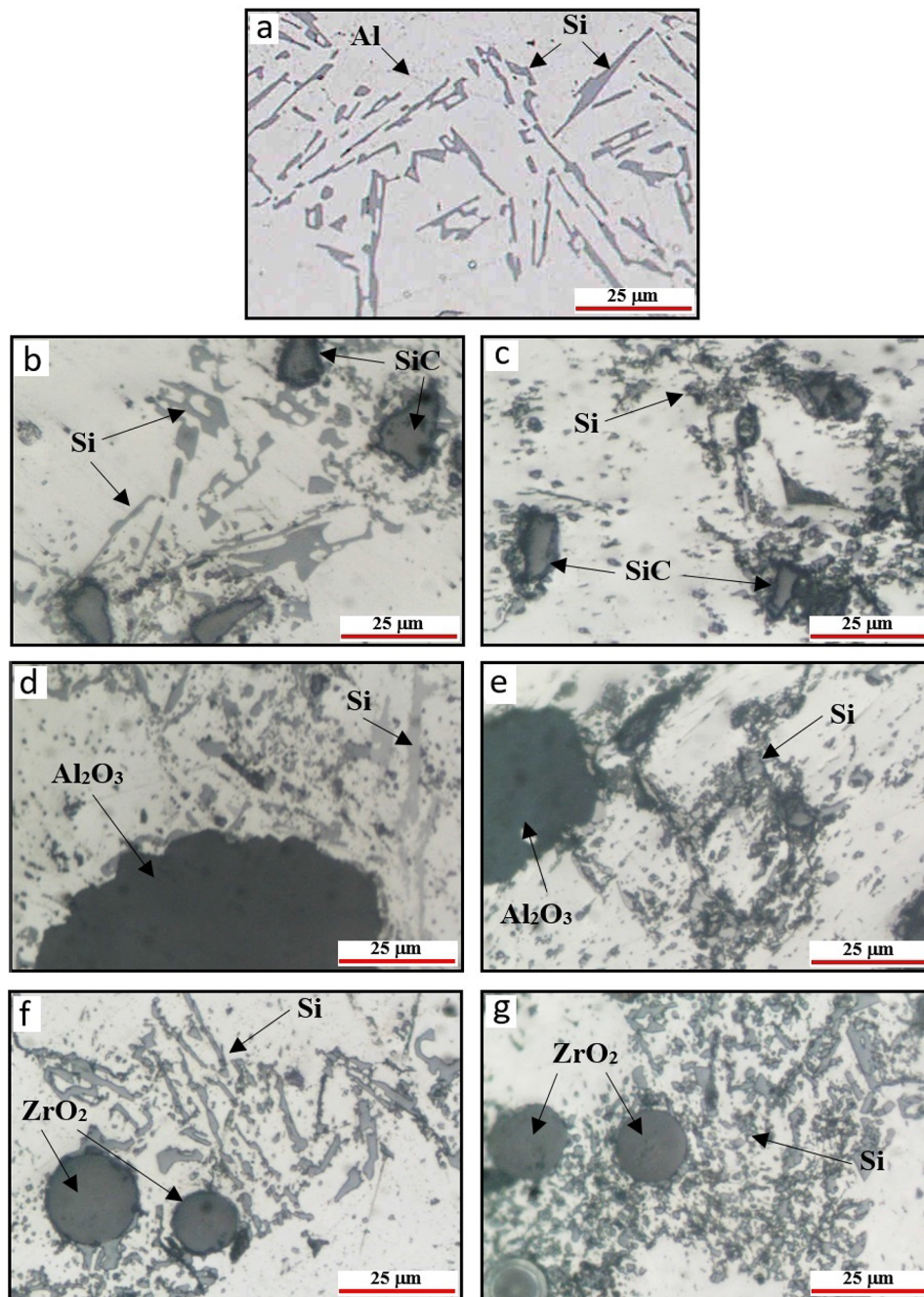


Figure 11. X-ray diffraction patterns of investigated composites.



**Figure 12. Optical microstructure of (a) A356.2 alloy, (b) A356.2/SiC, (c) A356.2+Bi/SiC, (d) A356.2/Al<sub>2</sub>O<sub>3</sub>, (e) A356.2+Bi/Al<sub>2</sub>O<sub>3</sub>, (f) A356.2/ZrO<sub>2</sub>, and (g) A356.2+Bi/ZrO<sub>2</sub> composites.**

primary  $\alpha$ -Al phase. Kim and Rohatgi<sup>23</sup> noted that the precipitation of the primary phase on the surfaces of ceramic particles in the melt is more favorable in hyper-eutectic Al-Si alloys than for hypoeutectic alloys. Therefore, Al<sub>2</sub>O<sub>3</sub>, ZrO<sub>2</sub>, and SiC particles do not act as nucleating agents for the primary  $\alpha$ -Al dendrites. Moreover, eutectic Si appears as coarse and flake-like morphology. The structure of eutectic Si significantly affects the mechanical properties of Al-Si alloys. Figure 12b shows the microstructure of the A356.2/SiC composite. It can be seen that SiC particles integrated into the matrix and

were found to lay in the eutectic region. This is because particulate reinforcements are generally segregated in the last freezing zone during solidification and rejected by the solidifying primary  $\alpha$ -Al phase. This effect is known as the particle-pushing phenomenon.<sup>34,39</sup> After adding Bi, eutectic Si transforms to a more refined shape in the form of a lamellar structure in A356.2+Bi/SiC composite (Figure 12c). Figure 12d and e shows the microstructure of A356.2/Al<sub>2</sub>O<sub>3</sub> and A356.2+Bi/Al<sub>2</sub>O<sub>3</sub>, respectively. Al<sub>2</sub>O<sub>3</sub> particles were seen to be incorporated into the aluminum matrix. Moreover, Si's flake and sharp nature were

transformed into a shorter and more refined structure. The microstructure of A356.2/ZrO<sub>2</sub> is shown in Figure 12f. ZrO<sub>2</sub> particles are located in the eutectic region, the last freezing zone in hypoeutectic Al-Si alloys.

Against Samuel's finding,<sup>40</sup> no sign of eutectic Si refinement was observed after adding SiC, Al<sub>2</sub>O<sub>3</sub>, and ZrO<sub>2</sub> reinforcements into the A356.2 matrix alloy. Perhaps, it is for this reason that Rohatgi and his colleagues<sup>41</sup> concluded that further study is needed to quantify the effect of particles on the nucleation and growth of phases during the solidification of composite.

Figure 12g shows the A356.2/ZrO<sub>2</sub> composite's microstructure after adding Bi. It can be seen that the morphology of eutectic Si changed to the refined structure after adding the Bi. It is clear from Figure 12c, e, and f that Bi has a refining effect on the shape and size of eutectic Si. It has been reported that Bi can modify the morphology of eutectic silicon from flake to lamellar crystal.<sup>42,43</sup> As shown in Figure 5, Bi addition induces lower eutectic growth temperature (T<sub>EG</sub>), and the system needs more activation energy to overcome the restriction of Si growth during solidification. These results contrast those previously reported in which the modification effect of Sr addition was lost due to the presence of SiC.<sup>14</sup> In addition, the area fraction of eutectic Si increases after refinement. This can lead to the engulfment of reinforcement particles by the growing eutectic Al-Si interfaces in the last pools of the liquid matrix, improving their distribution in the A356.2 matrix.

## Conclusions

In the present study, the influence of the addition of SiC, Al<sub>2</sub>O<sub>3</sub>, and ZrO<sub>2</sub> particles on the microstructural and solidification characteristics of A356.2 alloy with and without Bi addition is studied with the use of the Fourier thermal analysis method. The conclusions can be drawn as follows:

1. Microstructural observation and XRD analysis revealed that SiC, Al<sub>2</sub>O<sub>3</sub>, and ZrO<sub>2</sub> particles have been successfully embedded in the A356.2 matrix alloy.
2. The cooling rate increased from 0.8 °C/s to 1.9 °C/s after addition of SiC, Al<sub>2</sub>O<sub>3</sub>, and ZrO<sub>2</sub> particles.
3. The solidification temperature range increased by 5%; however, the solidification duration decreased by 21%.
4. The coherency point characteristics and solid fraction at coherency did not change remarkably after incorporating SiC, Al<sub>2</sub>O<sub>3</sub>, and ZrO<sub>2</sub> particles.
5. Adding Bi element to composites did not affect the freezing characteristic of the  $\alpha$ -Al phase. Still, it resulted in the depression of eutectic growth temperature and the refinement of eutectic Si.

6. The obtained data from thermal analysis and microstructure characterization of A356.2 and fabricated composites depict that reinforcement particles cannot act as nucleation agents for both  $\alpha$ -Al and eutectic Si.

## REFERENCES

1. P.K. Rohatgi, N. Gupta, A. Daoud, Synthesis and processing of cast metal-matrix composites and their applications, in: casting. ASM handb. (2008). <https://doi.org/10.31399/asm.hb.v15.a0005339>
2. V.V. Vani, S.K. Chak, The effect of process parameters in aluminum metal matrix composites with powder metallurgy. *Manuf. Rev.* (2018). <https://doi.org/10.1051/mfreview/2018001>
3. Ş Karabulut, U. Gökmen, H. Çinici, Study on the mechanical and drilling properties of AA7039 composites reinforced with Al<sub>2</sub>O<sub>3</sub>/B<sub>4</sub>C/SiC particles. *Compos. B Eng.* (2016). <https://doi.org/10.1016/j.compositesb.2016.02.054>
4. J. Cintas, F.G. Cuevas, J.M. Montes, E.J. Herrera, High-strength PM aluminium by milling in ammonia gas and sintering. *Scr. Mater.* **53**, 1165–1170 (2005). <https://doi.org/10.1016/J.SCRIPTAMAT.2005.07.019>
5. P.K. Rohatgi, R.Q. Guo, H. Iksan, E.J. Borchelt, R. Asthana, Pressure infiltration technique for synthesis of aluminum—fly ash particulate composite. *Mater. Sci. Eng. A* **244**, 22–30 (1998). [https://doi.org/10.1016/S0921-5093\(97\)00822-8](https://doi.org/10.1016/S0921-5093(97)00822-8)
6. X. Liu, S. Jia, L. Nastac, Ultrasonic cavitation-assisted molten metal processing of cast a356-nanocomposites. *Int. J. Metalcast.* **8**, 51–58 (2014). <https://doi.org/10.1007/BF03355591>
7. R. Mohammadi Badizi, M. Askari-Paykani, A. Parizad, H.R. Shahverdi, Effects of electromagnetic frequency and SiC nanoparticles on the microstructure refinement and mechanical properties of Al A357–1.5 wt% SiC nanocomposites. *Int. J. Metalcast.* **12**, 565–573 (2018). <https://doi.org/10.1007/s40962-017-0194-z>
8. N. Parumandla, K. Adepu, Effect of tool shoulder geometry on fabrication of Al/Al<sub>2</sub>O<sub>3</sub> surface nano composite by friction stir processing. *Part. Sci. Technol.* **38**, 121–130 (2020). <https://doi.org/10.1080/02726351.2018.1490361>
9. M. Shayan, B. Eghbali, B. Niroumand, Synthesis of AA2024-(SiO<sub>2</sub>np+TiO<sub>2</sub>np) hybrid nanocomposite via stir casting process. *Mater. Sci. Eng. A* (2019). <https://doi.org/10.1016/j.msea.2019.04.089>
10. A. Lakshmikanthan, S. Bontha, M. Krishna, P.G. Koppad, T. Ramprabhu, Microstructure, mechanical and wear properties of the A357 composites reinforced with dual sized SiC particles. *J. Alloys Compd.* (2019). <https://doi.org/10.1016/j.jallcom.2019.01.382>

11. S.A. Sajjadi, H.R. Ezatpour, M.T. Parizi, Comparison of microstructure and mechanical properties of A356 aluminum alloy/Al<sub>2</sub>O<sub>3</sub> composites fabricated by stir and compo-casting processes. *Mater. Des.* **34**, 106–111 (2012). <https://doi.org/10.1016/j.matdes.2011.07.037>
12. X. Du, T. Gao, D. Li, Y. Wu, X. Liu, A novel approach to synthesize SiC particles by in situ reaction in Al–Si–C alloys. *J. Alloys Compd.* **588**, 374–377 (2014). <https://doi.org/10.1016/J.JALLCOM.2013.11.099>
13. M.O. Shabani, A. Mazahery, The synthesis of the particulates Al matrix composites by the compocasting method. *Ceram Int.* (2013). <https://doi.org/10.1016/j.ceramint.2012.07.073>
14. J.C. Baez, C. Gonzalez, M.R. Chavez, M. Castro, J. Juarez, Fourier thermal analysis of the solidification kinetics in A356/SiCp cast composites. *J. Mater. Process. Technol.* **153–154**, 531–536 (2004). <https://doi.org/10.1016/J.JMATPROTEC.2004.04.119>
15. D.M. Stefanescu, Thermal analysis—theory and applications in metalcasting. *Int. J. Metalcast.* **9**, 7–22 (2015). <https://doi.org/10.1007/BF03355598>
16. T.P.D. Rajan, K. Narayan Prabhu, R.M. Pillai, B.C. Pai, Solidification and casting/mould interfacial heat transfer characteristics of aluminum matrix composites. *Compos. Sci. Technol.* (2007). <https://doi.org/10.1016/j.compscitech.2006.03.028>
17. O. Cabrera, M. Ramírez, B. Campillo, C. González-Rivera, Effect of the presence of SiCp on dendritic coherency of Al–Si-based alloys during solidification. *Mater. Manuf. Processes* (2008). <https://doi.org/10.1080/10426910701524493>
18. J. Braszczyński, A. Zyska, Analysis of the influence of ceramic particles on the solidification process of metal matrix composites. *Mater. Sci. Eng. A* (2000). [https://doi.org/10.1016/S0921-5093\(99\)00573-0](https://doi.org/10.1016/S0921-5093(99)00573-0)
19. A.E. Karantzalis, A. Lekatou, E. Georgatis, H. Mavros, Solidification behaviour of ceramic particle reinforced Al-alloy matrices. *J. Mater. Sci.* (2010). <https://doi.org/10.1007/s10853-009-4055-x>
20. R. Asthana, Reinforced cast metals: part I solidification microstructure. *J. Mater. Sci.* **33**, 1679–1698 (1998). <https://doi.org/10.1023/A:1004308027679>
21. J. Gan, J. Du, C. Wen, G. Zhang, M. Shi, Z. Yuan, The Effect of Fe Content on the Solidification Pathway, Microstructure and Thermal Conductivity of Hypoeutectic Al–Si Alloys. *Int. J. Metalcast.* **16**, 178–190 (2022). <https://doi.org/10.1007/s40962-021-00580-0>
22. C. Wen, J. Gan, C. Li, Y. Huang, J. Du, Comparative study on relationship between modification of Si phase and thermal conductivity of Al–7Si alloy modified by Sr/RE/B/Sb elements. *Int. J. Metalcast.* **15**, 194–205 (2021). <https://doi.org/10.1007/s40962-020-00436-z>
23. J.K. Kim, P.K. Rohatgi, Nucleation on ceramic particles in cast metal-matrix composites. *Metall. Mater. Trans. A* **31**, 1295–1304 (2000). <https://doi.org/10.1007/s11661-000-0124-0>
24. C. Gonzalez-Rivera, J. Baez, R. Chavez, A. García, J. Juarez-Islas, Quantification of the SiCp content in molten Al–Si/SiC p composites by computer aided thermal analysis. *J. Mater. Process. Technol.* (2003). [https://doi.org/10.1016/S0924-0136\(03\)00354-6](https://doi.org/10.1016/S0924-0136(03)00354-6)
25. S. Deepak Kumar, A. Mandal, M. Chakraborty, Solid fraction evolution characteristics of semi-solid A356 alloy and in-situ A356–TiB<sub>2</sub> composites investigated by differential thermal analysis. *Int. J. Miner. Metall. Mater.* (2015). <https://doi.org/10.1007/s12613-015-1084-0>
26. S.C. Jeng, S.W. Chen, The solidification characteristics of 6061 and a356 aluminum alloys and their ceramic particle-reinforced composites. *Acta Mater.* (1997). [https://doi.org/10.1016/S1359-6454\(97\)00189-4](https://doi.org/10.1016/S1359-6454(97)00189-4)
27. H. Ghandvar, S. Farahany, T.A. Abu Bakar, A novel method to enhance the performance of an ex-situ Al/Si-YSZ metal matrix composite. *J. Alloys Compd.* (2020). <https://doi.org/10.1016/j.jallcom.2020.153673>
28. S.B. Prabu, L. Karunamoorthy, S. Kathiresan, B. mohan, Influence of stirring speed and stirring time on distribution of particles in cast metal matrix composite. *J. Mater. Process. Technol.* (2006). <https://doi.org/10.1016/j.jmatprotec.2005.06.071>
29. D. Emadi, L.V. Whiting, S. Nafisi, R. Ghomashchi, Applications of thermal analysis in quality control of solidification processes. *J. Therm. Anal.* **81**, 235–241 (2005). <https://doi.org/10.1007/s10973-005-0772-9>
30. D. Emadi, L.V. Whiting, M. Djurdjevic, W.T. Kierkus, J. SOKOLOWSKI, Comparison of newtonian and fourier thermal analysis techniques for calculation of latent heat and solid fraction of aluminum alloys. *Metall. Mater. Eng.* (2018). <https://doi.org/10.30544/379>
31. S. Gowri, F.H. Samuel, Effect of cooling rate on the solidification behavior of Al–7 Pct Si–SiCp metal-matrix composites. *Metall. Trans. A* (1992). <https://doi.org/10.1007/BF02663446>
32. S. Farahany, A. Ourdjini, M.H. Idris, The usage of computer-aided cooling curve thermal analysis to optimise eutectic refiner and modifier in Al–Si alloys. *J. Therm. Anal. Calorim.* (2012). <https://doi.org/10.1007/s10973-011-1708-1>
33. S. Farahany, A. Ourdjini, T.A.A. Bakar, M.H. Idris, On the refinement mechanism of silicon in Al–Si–Cu–Zn alloy with addition of bismuth. *Metall. Mater. Trans. A Phys. Metall. Mater. Sci.* **45**, 1085–1088 (2014). <https://doi.org/10.1007/s11661-013-2158-0>
34. C. Gonzalez-Rivera, J. Baez, R. Chavez, O. Alvarez, J. Juarez-Islas, Effect of SiC<sub>p</sub> content on cooling curve characteristics and solidification kinetics of Al–Si/SiC<sub>p</sub> cast composites. *Int. J. Cast Met. Res.* **16**, 531–536 (2003). <https://doi.org/10.1080/13640461.2003.11819631>

35. G.S. Hanumanth, G.A. Irons, Solidification of particle-reinforced metal-matrix composites. *Metall. Mater. Trans. B* **27**, 663–671 (1996). <https://doi.org/10.1007/BF02915665>
36. G. Chai, L. BÄckerud, T. RØlland, L. Arnberg, Dendrite coherency during equiaxed solidification in binary aluminum alloys. *Metall. Mater. Trans. A* **26**, 965–970 (1995). <https://doi.org/10.1007/BF02649093>
37. M. Malekan, S.G. Shabestari, Effect of grain refinement on the dendrite coherency point during solidification of the A319 aluminum alloy. *Metall. Mater. Trans. A* **40**, 3196 (2009). <https://doi.org/10.1007/s11661-009-9978-y>
38. V.E. Bazhenov, Av. Petrova, Av. Sannikov, A.A. Rizhsky, AYu. Titov, Y. Tselovalnik, DYu. Ozherelkov, I.N. Pashkov, Av. Koltygin, V.D. Belov, Relationship between critical solid fraction and dendrite coherency point in Al–Si alloys. *Int. J. Metalcast.* (2022). <https://doi.org/10.1007/s40962-022-00772-2>
39. J.K. Kim, P.K. Rohatgi, The effect of the diffusion of solute between the particle and the interface on the particle pushing phenomena. *Acta Mater.* **46**, 1115–1123 (1998). [https://doi.org/10.1016/S1359-6454\(97\)00331-5](https://doi.org/10.1016/S1359-6454(97)00331-5)
40. A.M. Samuel, F.H. Samuel, Influence of casting and heat treatment parameters in controlling the properties of an Al-10 wt% Si-0.6 wt% Mg/SiC/20p composite. *J. Mater. Sci.* **29**, 3591–3600 (1994). <https://doi.org/10.1007/BF00357323>
41. P.K. Rohatgi, P. Ajay Kumar, N.M. Chelliah, T.P.D. Rajan, Solidification processing of cast metal matrix composites over the last 50 years and opportunities for the future. *JOM* **72**, 2912–2926 (2020). <https://doi.org/10.1007/s11837-020-04253-x>
42. A.M.A. Mohamed, F.H. Samuel, A.M. Samuel, H.W. Doty, Effects of individual and combined additions of Pb, Bi, and Sn on the microstructure and mechanical properties of Al-10.8Si-2.25Cu-0.3Mg alloy. *Metall. Mater. Trans. A* **40**, 240–254 (2009). <https://doi.org/10.1007/s11661-008-9692-1>
43. S. Farahany, A. Ourdjini, T.A. Abu Bakar, M.H. Idris, A new approach to assess the effects of Sr and Bi interaction in ADC12 Al-Si die casting alloy. *Thermochim. Acta* **575**, 179–187 (2014). <https://doi.org/10.1016/j.tca.2013.11.001>

**Publisher’s Note** Springer Nature remains neutral with regard to jurisdictional claims in published maps and institutional affiliations.

Springer Nature or its licensor (e.g. a society or other partner) holds exclusive rights to this article under a publishing agreement with the author(s) or other rightsholder(s); author self-archiving of the accepted manuscript version of this article is solely governed by the terms of such publishing agreement and applicable law.